The Dawn of Disk Formation in a Milky Way-sized Galaxy Halo: Thin Stellar Disks at $z > 4$

Tomas Tamfal[1] , Lucio Mayer[1] , Thomas R. Quinn[2] , Arif Babul[3] , Piero Madau[4] , Pedro R. Capelo[1] ,
Sijing Shen[5] , and Marius Staub[6]

[1] Center for Theoretical Astrophysics and Cosmology, Institute for Computational Science, University of Zurich, Winterthurerstrasse 190, CH-8057 Zürich, Switzerland; tomas.tamfal@uzh.ch
[2] Astronomy Department, University of Washington, Seattle, WA 98195, USA
[3] Department of Physics & Astronomy, University of Victoria, BC, V8X 4M6, Canada
[4] Department of Astronomy & Astrophysics, University of California, 1156 High Street, Santa Cruz, CA 95064, USA
[5] Institute of Theoretical Astrophysics, University of Oslo, Postboks 1029, NO-0315 Oslo, Norway
[6] Institute for Particle Physics and Astrophysics, Eidgenössische Technische Hochschule, Wolfgang-Pauli-Strasse 27, 8049 Zürich, Switzerland

Abstract

We present results from GIGAERIS, a cosmological, N-body hydrodynamical "zoom-in" simulation of the formation of a Milky Way-sized galaxy halo with unprecedented resolution, encompassing of order a billion particles within the refined region. The simulation employs a modern implementation of smoothed-particle hydrodynamics, including metal-line cooling and metal and thermal diffusion. We focus on the early assembly of the galaxy, down to redshift $z = 4.4$. The simulated galaxy has properties consistent with extrapolations of the main sequence of star-forming galaxies to higher redshifts and levels off to a star formation rate of $\sim 60\,M_\odot\,\mathrm{yr}^{-1}$ at $z = 4.4$. A compact, thin rotating stellar disk with properties analogous to those of low-redshift systems arises already at $z \sim 8$. The galaxy rapidly develops a multi-component structure, and the disk, at least at these early stages, does not grow "upside-down" as often reported in the literature. Rather, at any given time, newly born stars contribute to sustain a thin disk. The kinematics reflect the early, ubiquitous presence of a thin disk, as a stellar disk component with v_ϕ/σ_R larger than unity is already present at $z \sim 9$–10. Our results suggest that high-resolution spectro-photometric observations of very high-redshift galaxies should find thin rotating disks, consistent with the recent discovery of cold rotating gas disks by ALMA. Finally, we present synthetic images for the James Webb Space Telescope NIRCam camera, showing how the early disk would be easily detectable already at those early times.

1. Introduction

The origin of the thin and thick disks of present-day spirals, most notably the Milky Way, has been the subject of intense debate in recent decades. Various mechanisms have been proposed to produce a thick disk out of the thin disk, which have been tested primarily via observations of the Milky Way, including heating by merging satellites, internal dynamical heating by buckling bars, and accretion of lower angular momentum stars from satellites themselves (see Gilmore et al. 1989; Quinn et al. 1993; Wyse 2001; Abadi et al. 2003; Meza et al. 2005; Wyse et al. 2006; Villalobos & Helmi 2008; Purcell et al. 2009; Di Matteo et al. 2011). These mechanisms all play a role to some extent. On the numerical simulations side, in the last decade cosmological hydrodynamical simulations using the "zoom-in" technique have reached enough realism to be able to capture quite faithfully all these processes, as well as the re-formation of thin disk components from subsequent gas accretion episodes, especially at lower redshift, when gas accretes on higher angular momentum orbits (Bird et al. 2013, 2021; Grand et al. 2016; Wetzel et al. 2016;

El-Badry et al. 2018; Hopkins et al. 2018; Hafen et al. 2019). Overall, simulations seem to have no more issues in producing a variety of disk galaxies whose disk structure resembles real ones (Grand et al. 2016; Sokołowska et al. 2017). Such simulations also predict that, at high redshift, the early disk component is thick as the gas accretes in a rather turbulent environment with many mergers occurring in relatively short timescales and along different planes (Bird et al. 2013).

This has led to the notion that the disk forms "upside-down", namely the extended thin disk forms only at a later stage, when gas accretes along smoother, higher angular momentum filaments. Recently, however, observations with ALMA and other instruments have revealed the existence of rotationally supported disks of gas at very high redshift, raising the question of whether this is consistent or not with the "upside-down" scenario (e.g., Hodge et al. 2019; Le Fèvre et al. 2020; Neeleman et al. 2020; Rizzo et al. 2020). And indeed, lately new studies have shown that such a (gaseous) disk can also be found in numerical simulations (see Meng et al. 2019; Meng & Gnedin 2021; Kretschmer et al. 2022). The importance of both mass and spatial resolution in understanding galaxy formation at low redshift, and in particular the assembly of the galactic disk component, has been shown clearly by the way progress has occurred throughout the 2000s (e.g., Kaufmann et al. 2007; Mayer et al. 2008; Governato et al. 2010). Similar issues might

now be relevant to understand galaxy formation at much higher redshift.

Here, we revisit the problem of early disk assembly with a "zoom-in" cosmological hydrodynamical simulation of unprecedented resolution, GIGAERIS. Compared to predecessor runs such as those of the ERIS suite, which were originally used to develop the scenario of "upside-down" disk formation (Bird et al. 2013), GIGAERIS has a mass resolution nearly 20 times better, yielding a typical hydrodynamical spatial resolution of a few parsecs as opposed to tens of parsecs in previous simulations. Compared to the most recent "zoom-in" simulations of Milky Way-sized galaxy halos in the FIRE-2 and ELVIS-ON-FIRE suites (Garrison-Kimmel et al. 2014, 2019; Santistevan et al. 2021), the gas mass resolution in GIGAERIS is, respectively, eight times and four times better. This allows us to probe the early stages of galaxy formation with much greater physical realism than before, when the progenitors of present-day Milky Way-like galaxies have a baryonic and dark matter (DM) mass considerably smaller than at the present day. Equipped with such resolution, we can address whether the absence of a thin disk at high redshift in previous simulated galaxies is a physical result or the consequence of numerical limitations during the early stages of galaxy assembly which degrade the resolution of the scale height of the cold interstellar medium.

The paper is divided in four parts which are organized as follows: methods, results, discussion, and a summary section. Furthermore, the results section is again divided in three parts: a subsection about the evolution of the main galaxy as well as a comparison with previous work and observations, a subsection about the thin disk, and a subsection on the multiple formation mechanisms at high redshift.

2. Methods

2.1. Simulation Code

The simulation was evolved with the collisionless N-body smoothed-particle hydrodynamics (SPH) Charm N-body GrAvity solver (CHANGA; see Jetley et al. 2008, 2010; Menon et al. 2015). The code uses a Barnes & Hut (1986) oct-tree to calculate gravity, with hexadecapole expansion of nodes and Ewald (1921) summation for periodic forces. It follows the gas dynamics using a modern implementation of the SPH method, adopting a Wendland C4 kernel (Wendland 1995; Dehnen & Aly 2012; Keller et al. 2014), a geometric density average force calculation, and turbulent diffusion of thermal energy, as well as metal diffusion (Wadsley et al. 2017). The timestepping in CHANGA is carried out with a leapfrog integrator using individual timesteps for every particle. Each individual stellar particle represents an entire stellar population following the initial mass function described in Kroupa (2001), with an initial particle mass of $m_\star = 1026\ M_\odot$. We form stars stochastically using a simple gas density and temperature threshold criterion, with $n_{SF} > 100$ atoms cm^{-3} and $T < 3 \times 10^4$ K, and with a star formation rate given by

$$\frac{d\rho_\star}{dt} = \epsilon_{SF} \frac{\rho_{gas}}{t_{dyn}}, \qquad (1)$$

with $\rho_\star$ denoting the stellar density, ρ_{gas} the gas density, t_{dyn} the local dynamical time, and $\epsilon_{SF} = 0.1$ the star formation efficiency. We also apply self-shielding (see Pontzen et al. 2008) and a redshift-dependent ultraviolet (UV) radiation background (Haardt & Madau 2012). In GIGAERIS, we solve for the non-equilibrium abundances of H and He ions, while cooling from fine-structure lines of metals at all temperatures (between 100 and 10^9 K) is calculated in photoionization equilibrium using tabulated rates from CLOUDY (see Ferland et al. 1998, 2013), following the method described in Shen et al. (2010, 2013). Feedback from Type Ia supernovae is implemented via stellar winds, whereas that from Type II supernovae is implemented following the delayed-cooling recipes of Stinson et al. (2006), and injecting metals and $\epsilon_{SN} = 10^{51}$ erg per event into the interstellar medium. The simulation used nearly 50 million core hours on the hybrid CPU+GPU nodes of the supercomputer Piz Daint at the Swiss National Supercomputing Centre (CSCS) and reached a final redshift of $z = 4.44$.

2.2. Initial Conditions

In this work, we follow a galactic-scale halo identified at $z = 0$ in a periodic cube of side 90 comoving Mpc (hereafter cMpc). We re-simulate the selected halo at several orders of magnitude higher resolution than the DM-only simulation, adding gas particles as well as the necessary short-wavelength modes, by tracing back the particles in an appropriately defined Lagrangian volume surrounding it, from $z = 300$ until redshift $z = 4.44$ ($\approx$1.4 Gyr after the big bang). The galaxy halo was selected in a similar way as in the original ERIS suite (Guedes et al. 2011; Sokołowska et al. 2017), namely as one with a quiet merging history (last major merger at $z \sim 2$) and average spin parameter (0.045), with a halo virial mass similar to but slightly larger than that of ERIS at $z = 0$, $1.4 \times 10^{12} M_\odot$. At the early epochs that are the focus of this paper, the galaxy is located in one major filament (Figure 1). The initial conditions were created with the MUSIC code (see Hahn & Abel 2011), using 14 levels of refinement and the cosmological parameters $\Omega_m = 0.3089$, $\Omega_b = 0.0486$, $\Omega_\Lambda = 0.6911$, $\sigma_8 = 0.8159$, $n_s = 0.9667$, and $H_0 = 67.74$ km s^{-1} Mpc^{-1} (Planck Collaboration et al. 2016). The Lagrangian region for the high-resolution region was chosen to be an ellipsoid with a semiminor axis of approximately 1.8 cMpc and a semimajor axis of 5 cMpc. The gravitational softening was chosen to be constant in physical coordinates for redshifts smaller than $z = 10$, $\epsilon_C = 0.043$ kpc, and otherwise to evolve as $\epsilon = 11\epsilon_C/(1 + z)$. For the final snapshot at $z = 4.44$, the particle numbers in the entire simulation are $n_{DM} = 5.7 \times 10^8$, $n_{gas} = 5.2 \times 10^8$, and $n_\star = 4.4 \times 10^7$, which leads to more than a billion (1.1×10^9) particles. At the same time, within the virial radius, we obtain $m_{DM} = 5493\ M_\odot$ and $n_{DM} = 4.2 \times 10^7$ for DM, a mean gas mass of $m_{gas} = 1099\ M_\odot$ and $n_{gas} = 1.1 \times 10^7$, and a mean stellar mass of $m_\star = 798\ M_\odot$ and $n_\star = 3.9 \times 10^7$. Note that with our simulation design the refined simulation volume is large enough to allow following the galaxy until $z = 0$ without contamination by low-resolution particles.

2.3. Halo Finding

In order to find the main halo and also other substructures, we used the AMIGA Halo Finder (hereafter AHF; Gill et al. 2004; Knollmann & Knebe 2009) and applied it to our simulation box with a minimum of 1000 DM particles, 10 star particles, and 10 gas particles per halo.
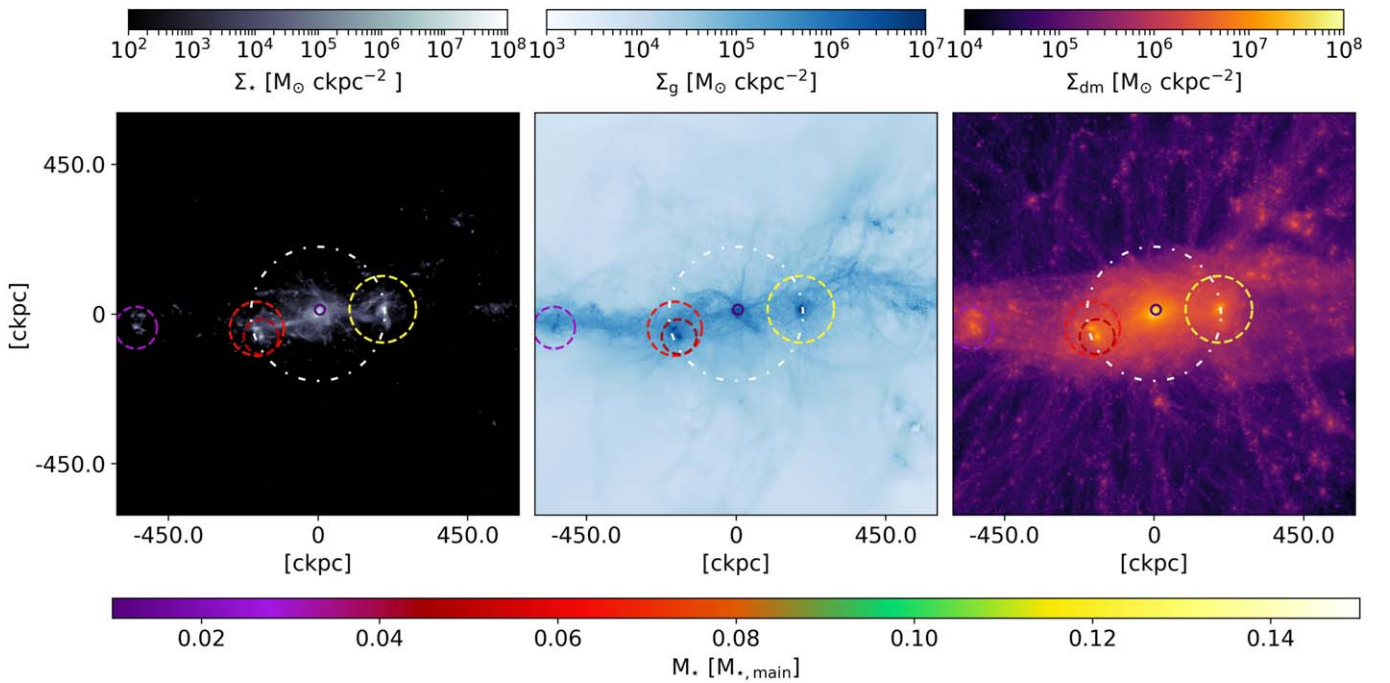
Figure 1. Main halo of the GIGAERIS simulation at $z = 4.44$. The left-hand panel shows the stellar surface density, the middle panel shows the gas surface density, and the right-hand panel depicts the dark matter surface density, all in units of $M_\odot$ ckpc^{-2} (see top colorbars). The white, dashed–dotted circle depicts the virial radius of the main galaxy. The other circles depict the virial radii of subhalos and are solid if the entire subhalo is within the main halo's virial radius or dashed if it is partially outside. The colorbar of the circles (see bottom bar) indicates the mass ratio between the stellar mass of the main halo and that of the subhalo.

3. Results

The primary system is a star-forming main-sequence galaxy with a relatively quiescent merger history residing in a large filament, with other converging secondary filaments (see Figure 1). In this study, we define a major merger as one with a mass ratio $q = M_{\rm sat}/M_{\rm halo} > 0.1$. In Figures 2 and 3 (top panels; dashed vertical lines), we show the times of the last 10 mergers, although from $z = 68$ to 4.44 we can count 14 major mergers, of which four have $q > 0.25$. At the final redshift, $z = 4.44$, the main halo has a virial radius of 37 kpc, a virial DM mass of $2.3 \times 10^{11}\ M_\odot$, a virial stellar mass of $3.1 \times 10^{10}\ M_\odot$, and a virial gas mass of $1.3 \times 10^{10}\ M_\odot$ (from the AHF output file). In Figure 2, we also show the distribution of the enclosed DM mass which shows a steep rise in the central region, although the total potential in the center is dominated by the stellar contribution out to ≈ 30 kpc. The galaxy grows quickly in mass, with its total mass being already well above $10^{11}\ M_\odot$ at $z \sim 6.5$. Interestingly, at this point the mass is comparable to that of the main galaxy in another zoom-in run performed with nearly identical hydrodynamical solver and sub-grid physics, the PONOS-HR simulation described in Fiacconi et al. (2017). However, the halo in that simulation, by the present time, is nearly six times more massive than that of GIGAERIS (an early-type galaxy, rather than a spiral, forms in a lower-resolution version of the PONOS-HR simulation by low redshift; see Ardila et al. 2021). The baryonic matter increases significantly its relative weight in the mass budget within the inner 10–20 kpc between $z \sim 7$ and $z \sim 4$. In Figure 3, we show that our galaxy lies on the main sequence (see top panel) and that the star formation history is in good agreement with observations from the VIMOS Ultra-Deep Survey (Tasca et al. 2015), which is a spectroscopic redshift survey of faint galaxies mainly in the redshift range $4.5 < z < 5.5$ (see bottom panel). Furthermore, we also show the result from PONOS-HR as a blue square

(see bottom panel), which highlights the similarities between these two simulations.

3.1. Disk Formation and Dynamics of Newly Born Stars

A first remarkable finding can be already seen in Figure 4, which shows the stellar surface density maps, which are divided into four rows and four columns. The maps are oriented face-on (second and fourth row) and edge-on (first and third row) on the whole stellar component of the simulation. The stellar surface densities are divided in formation time bins, analogously to the procedure described in Bird et al. (2013), but with a finer bin width. The interesting result is that, already by visual inspection, a flattened disk component, in which the bulk of the mass has a height below 300 pc, is already present at $z \sim 7$–8 (see Figure 4). The vertical extent of this disk is thus comparable to the present-day thin-disk component of spiral galaxies, and is quantified later in Figure 12. The stellar disk is rather compact in radial size at this redshift, though, as it extends out to no more than 1 kpc. The compact size reflects the small virial radius of the host halo, which indirectly imposes a ceiling on the orbital angular momentum of baryonic matter that can be gravitationally bound to the halo and cool down to form a disk (White & Rees 1978; Efstathiou & Jones 1980). The overall aspect ratio of the disk (scale height/disk scale length) is therefore larger than in present-day counterparts. The newborn stars have a similar aspect ratio even at this early time, but this becomes increasingly smaller, with the ratio between vertical and radial scale length reaching a value < 10 by $z < 5$, more akin to the thin disk in present-day spirals (Figures 4 and 5). This thin disk, due to our limited time evolution, may or may not be the seed of the galactic scale disk that the ERIS system eventually develops. It is possible that such a thin disk might form and subsequently be disrupted during the early course of galaxy evolution. But since our
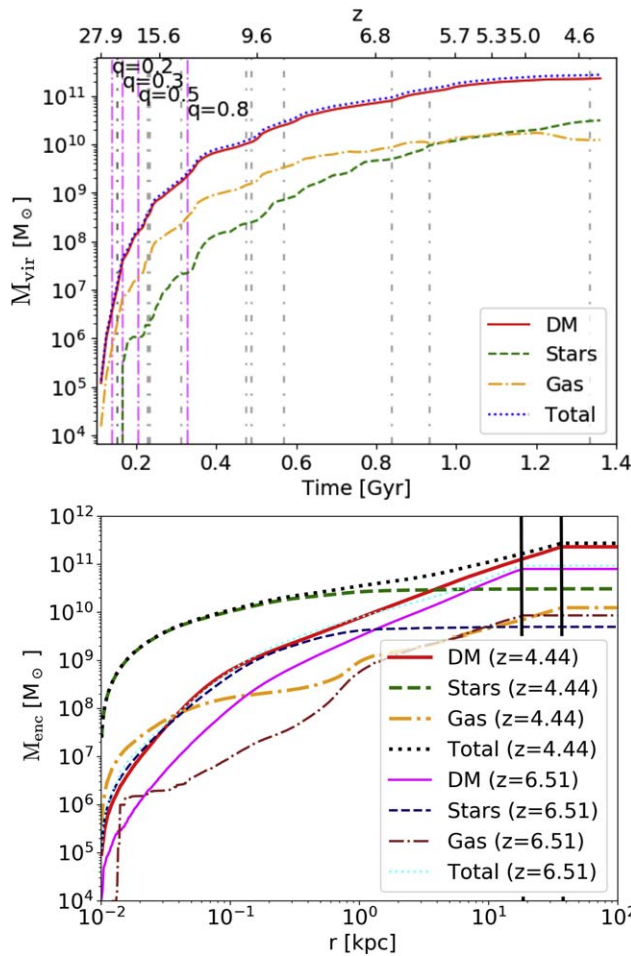
Figure 2. Bottom panel: enclosed mass of individual components as a function of radius at the end of our simulation ($z = 4.44$) and at $z = 6.51$: total mass (black and cyan, respectively), dark matter mass (red and magenta), stellar mass (green and navy), as well as gas mass (orange and brown). The two solid black vertical lines show the virial radius of the halo at the two selected redshifts. Top panel: enclosed mass, within the virial radius, of individual components as a function of time using the same color coding. The dashed vertical lines depict mergers with a mass ratio $q \equiv M_{sat}/M_{halo} > 0.1$ and the magenta lines highlight mergers with $q > 0.25$.

Figure 3. Top panel: star formation rate (left-hand y-axis, blue curve) and specific star formation rate (right-hand y-axis, red curve) of the stars within a [6 kpc $\times$ 6 kpc $\times$ 4 kpc] central box of the main galaxy as a function of redshift. The vertical lines depict major mergers ($q > 0.1$). Bottom panel: specific star formation rate (of the same subset of the top panel) as a function of stellar mass and color-coded with halo redshift. The VIMOS Ultra-Deep Survey survey data for galaxies in the redshift range $4.5 < z < 5.5$ (see Tasca et al. 2015) are depicted as black stars (with a redshift determination that is $\approx 70\%$–75% reliable) and red crosses (redshift determination is $\approx 100\%$ reliable). This figure shows also the result of the PONOS-HR simulation at redshift $z = 6.5$ as a blue square (from Fiacconi et al. 2017).

galaxy has a rather quiescent merger history, with no major merger after $z = 3$, we come to the conclusion that this is indeed the origin of today's Milky Way's thin disk. Furthermore, a more extended stellar envelope surrounding the thin disk grows with time (see the transition from Figure 4 to Figure 5, which shows the surface densities at $z = 4.44$). In the following subsections, we will characterize the galaxy by means of its global properties, including their time evolution, trying to shed light on the origin and evolution of this ubiquitous thin-disk component.

We can now characterize the state of the stellar disk more in-depth, and compare it with previous work, such as Bird et al. (2013, 2021), by comparing the lower panels in Figure 5, in which we observe the same "inside-out" and "bottom-up" growth as previously shown by Bird et al. (2013). However, conversely to previous work, we find that there is always a high central density with a thin component that can be attributed to a young stellar disk. Furthermore, during the entire simulation, the density maps always exhibit a thin disk, and portray prominent morphological features such as a bar or a rotating disk. The latter seems less prominent at the final snapshot,
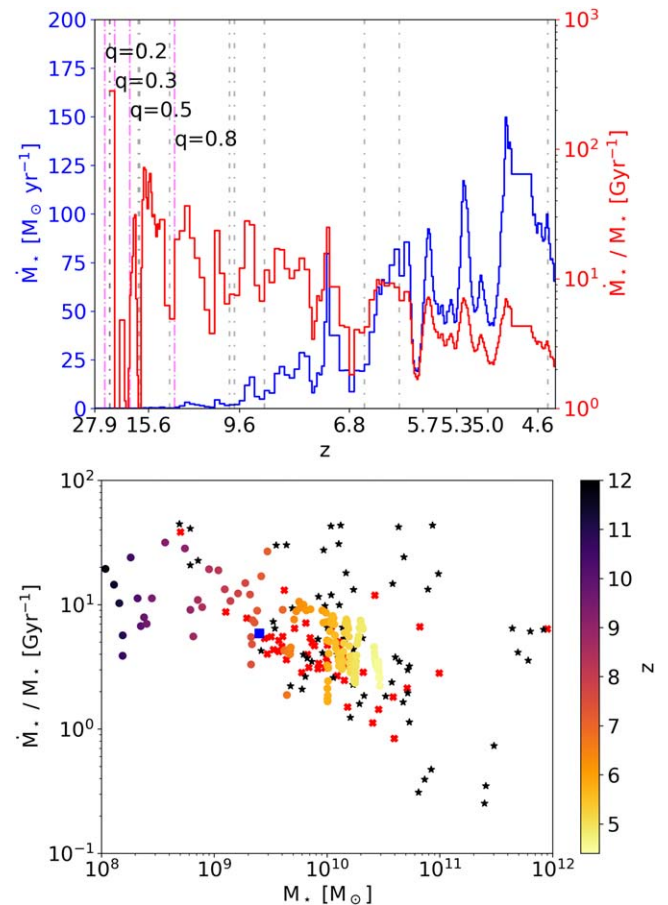
though these features can be easily seen at other times, such as at $z = 6.95$ (Figure 4).

To further demonstrate the existence of a thin disk even at high redshifts, we study the kinematics of the stars. We compute mean values of the rotational velocity v_ϕ and of the radial velocity dispersion σ_R. In particular, in Figure 6, we calculate the ratio of rotation to velocity dispersion $\langle v_\phi \rangle / \sigma_R$, which is a measure of how prominent a kinematically cold rotating disk of stars is. For this purpose, we consider particles in a cylinder with $r < 2$ kpc and -1 kpc $< z < 1$ kpc, binning them using the same formation time bins as in the surface density maps. We observe that, for all age cohorts, the profile peaks at a high value above unity and then decreases as time progresses. In addition, profiles for stars selected with increasingly younger ages peak at progressively larger values, reaching even above 5, as expected from "inside-out" disk formation bringing in progressively higher angular momentum baryons as more time elapses (Bird et al. 2013; Sokołowska et al. 2017). This is consistent with the low-redshift analysis of stellar kinematics for stars of different age cohorts made by Bird et al. (2013, 2021).
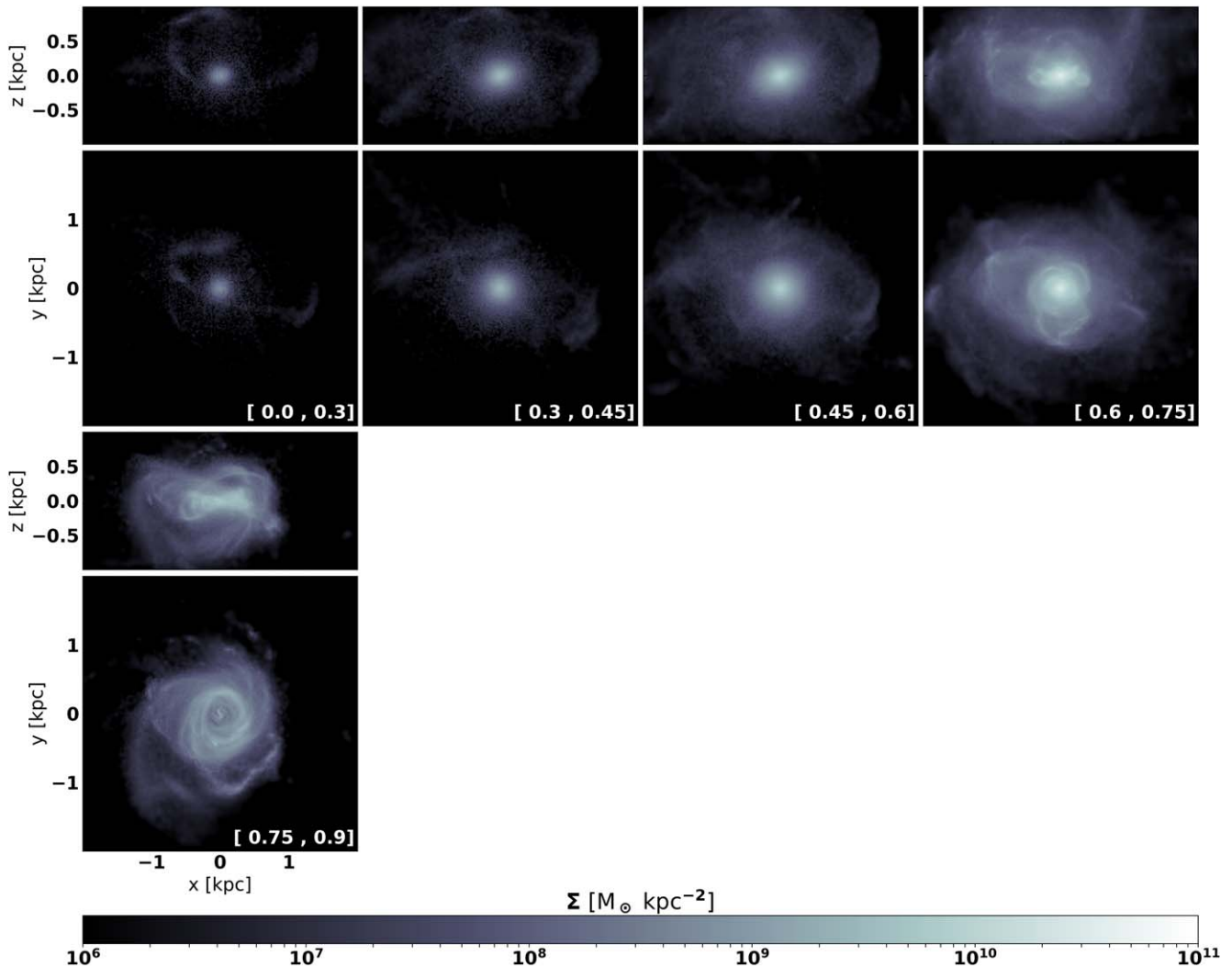
Figure 4. Stellar surface density maps at $z = 6.95$, approximately 0.77 Gyr after the big bang. The maps are oriented "edge-on" (top panels) and "face-on" (bottom panels), with the total stellar angular momentum along the z-axis, and afterwards split in various formation time bins (in Gyr). Each row shows surface densities in different bins associated to varying star formation time intervals, ranging from 0–0.3 Gyr (top left) to 0.75–0.9 Gyr after the big bang (bottom left). We should note that the disk, as can be inspected by the edge-on surface density maps, has a relatively large aspect ratio, which is at variance with present-day thin disks. However, the vertical extent of the disk, in the range 500–600 pc, does correspond to a present-day thin disk (e.g., Jurić et al. 2008), which is why here, and throughout the text, we refer to it as a thin disk.

We find that, concurrently, the rotational velocity itself always increases with time, growing from less than $100 \, \mathrm{km \, s^{-1}}$ at $z \sim 10$ to more than $300 \, \mathrm{km \, s^{-1}}$ toward $z \sim 4$. Therefore, the fact that the $\langle v_\phi \rangle / \sigma_R$ tends to decrease with time for the individual age cohorts, as shown in Figure 6, must be due to an increase in stellar velocity dispersion. The latter can be attributed to a variety of agents. Both accretion of stars with similar age but hotter kinematics, occurring through the many minor mergers impinging on the galaxy after $z = 10$ (see Figure 2), and heating of in situ stars by internal dynamical instabilities and perturbations by incoming massive satellites, can be responsible.

Among the internal heating mechanisms, there are disk thickening due to bar formation, which could play a role as a strong bar is seen to develop at $z < 6$ (the formation and evolution of a strong bar will be the topic of an upcoming paper), and various formation planes. The development of the bar is reflected in the evolution of the stellar surface density profile shown in Figure 7. Indeed, at $z < 6$ the profile becomes much steeper inside 0.5 kpc, which corresponds roughly to the

extent of the bar. This reflects outward transport of angular momentum by the bar, which generates a nuclear gas inflow and nuclear star formation (see, e.g., Debattista et al. 2006; Guedes et al. 2013). This result is at variance with previous high-resolution simulations at high redshift, such as PONOS-HR (run down to $z = 6.5$; Fiacconi et al. 2017), which exhibited nearly perfect exponential profiles. We caution, however, that bar formation is very sensitive to slight changes in the potential, as shown by the appearance of the bar in another version of the PONOS-HR simulation run to lower redshift (Bortolas et al. 2020). In order to quantify bar-driven heating or other internal heating mechanisms, though, the first step is to quantify, in general, how significant is the heating of in situ stars, namely separating out the presumably kinetically hotter stars that are gradually added as accretion and merging continues. This will be studied in detail in the next subsection, in which we will present a robust way to identify in situ disk components.

As we have just discussed, from the $\langle v_\phi \rangle / \sigma_R$ values (see Figure 6) we have clear evidence of a kinematically cold disk at
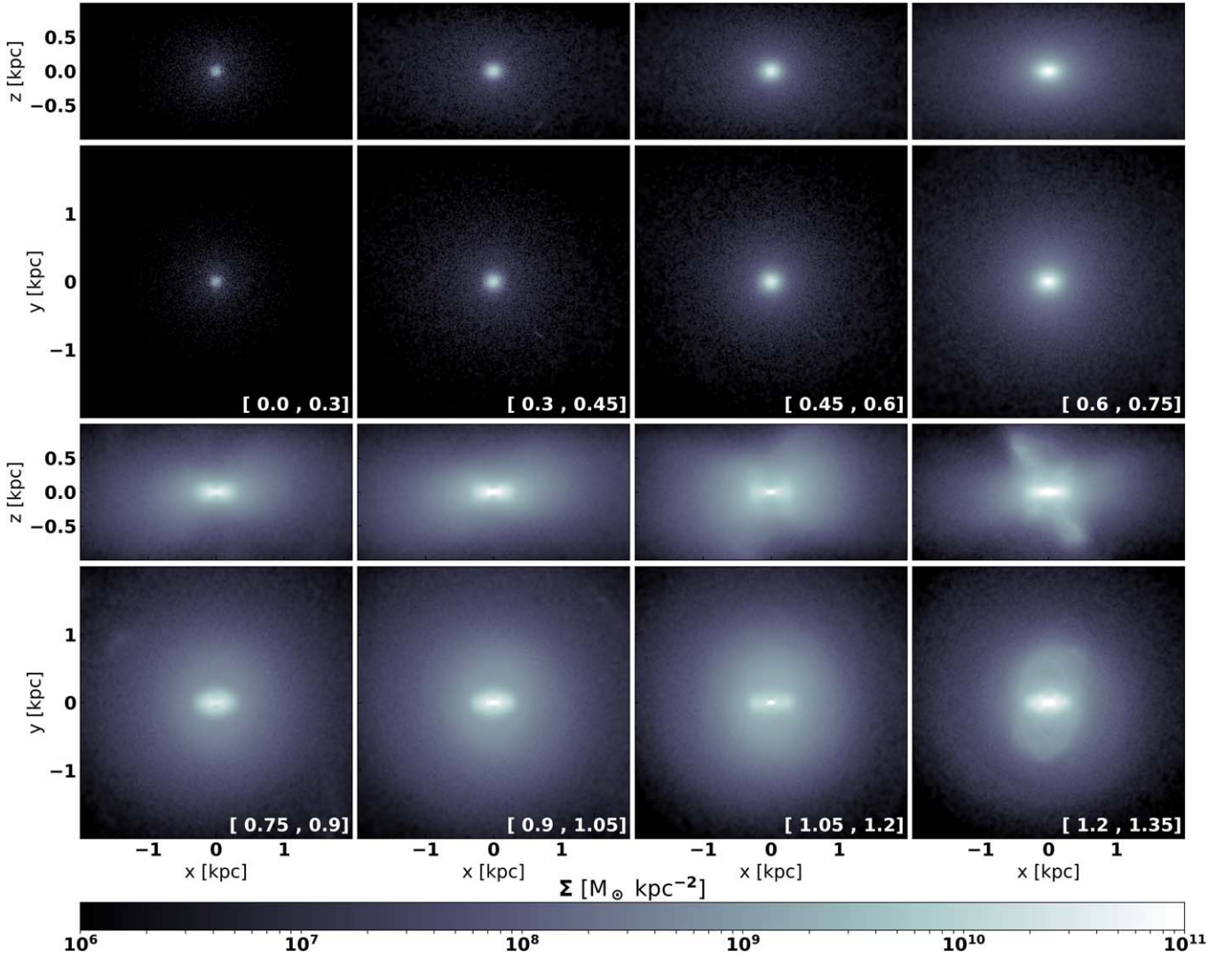
Figure 5. Same as Figure 4, but at $z = 4.44$; the maps are oriented "edge-on" (top panels) and "face-on" (bottom panels), with the total stellar angular momentum along the z-axis, and afterwards split in various formation time bins (in Gyr). In contrast to Figure 4, this figure is created at the final snapshot of the simulation and therefore the associated star formation time intervals are now ranging from 0–0.3 Gyr (top left) to 1.2–1.35 Gyr after the big bang (bottom right). Choosing a later time for this plot changes the interpretation, in contrast to Figure 4, strikingly; we now do not obtain a thin disk forming (lower two rows of the plot) but a rather thick structure which seems to confirm the picture given in Bird et al. (2013). This can be attributed to the fact that we now have additional stars in the disk that could have been born ex situ and therefore also change the visual appearance of each time bin.

any redshift. In order to further characterize the physical properties of this, we now compute the Toomre Q parameter (Toomre 1964). We do this for both the stellar and gas particles within a cylinder of 2 kpc height and radius of 2 kpc:

$$Q = \frac{\kappa V}{AG\Sigma}, \qquad (2)$$

with $\kappa = \sqrt{2(v_\phi/R)^2(1 + d\log v_\phi/d\log R)}$, $A = A_g = \pi$ and $A = A_\star = 3.36$, $V = V_\star = \sigma_R$ and $V = V_g = c_S$ (or, for turbulent gas, $V = V_g = \sqrt{c_S^2 + \sigma_{g,R}^2}$ (where c_S is the speed of sound). Furthermore, we also corrected for disk thickness, by multiplying Q by

$$T = \begin{cases} 1 + 0.6(\sigma_z/\sigma_R)^2 & \sigma_z/\sigma_R < 1/2, \\ 0.8 + 0.7(\sigma_z/\sigma_R) & \sigma_z/\sigma_R \geqslant 1/2, \end{cases} \qquad (3)$$

where we followed Romeo & Wiegert (2011; see also Romeo 1994; Romeo & Falstad 2013; Inoue et al. 2016).

We can write the Toomre Q parameter as

$$Q_{\text{tot}}^{-1} = \begin{cases} WQ_\star^{-1} + Q_g^{-1} & Q_\star \geqslant Q_g, \\ Q_\star^{-1} + WQ_g^{-1} & Q_\star < Q_g, \end{cases} \qquad (4)$$

with $W = 2V_\star V_g/(V_\star^2 + V_g^2)$ (again, see Romeo & Wiegert 2011). In Figure 8, we show the Toomre Q parameter and conclude that we have a stable stellar disk at $z \approx 6.44$, which is roughly the same time of the analysis in PONOS-HR (Fiacconi et al. 2017). The Toomre Q, however, is higher in PONOS-HR (see Section 4). Furthermore, at $z < 6$ the Q of the stars decreases significantly as the disk becomes unstable to bar formation, which in PONOS-HR (run down to $z = 6.5$; Fiacconi et al. 2017) is not observed. This likely reflects the higher stellar mass and relatively lower halo mass of GIGAERIS, which renders its disk more unstable to non-axisymmetric instabilities.
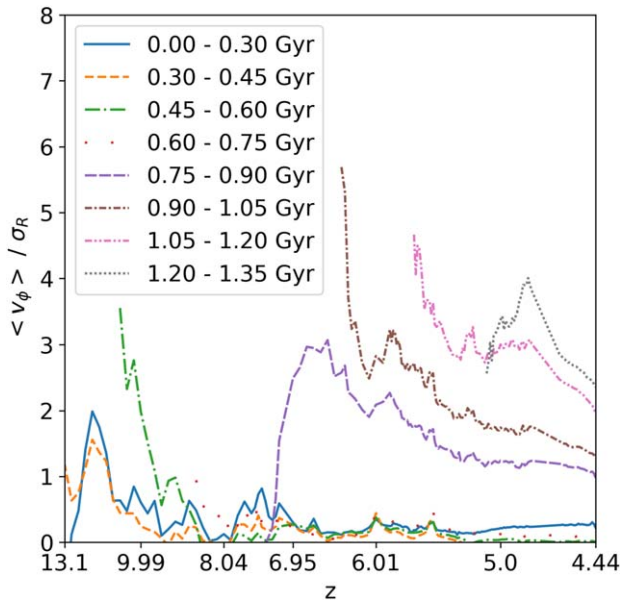
Figure 6. Mean circular velocity $\langle v_\phi \rangle$ divided by radial velocity dispersion σ_R, binned by different stellar formation times as a function of time. The binning of the formation time is chosen to be the same as in Figure 5. After 0.8 Gyr, stars are always born in a disk-like structure.
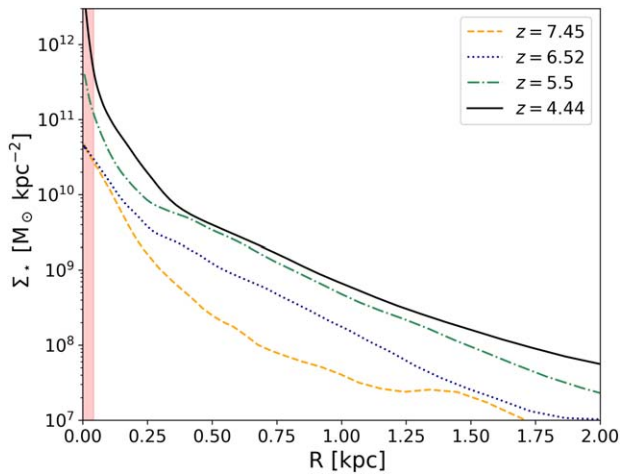

Figure 7. Stellar surface density profiles in the same radial range as in Fiacconi et al. (2017), for four different redshifts: $z = 7.45$, 6.52, 5.5, and 4.44. The red shaded region depicts the softening of our simulation.

Figure 8. Toomre Q parameter of stars (orange), gas (light blue), and turbulent gas (dark blue), and the total Q (black) as a function of radius at $z = 6.44$ (top panel) and at $z = 5.17$ (bottom panel). The shaded regions show the marginally stable (pink) and the unstable region (red). Even at $z = 6.44$, which is comparable with the PONOS-HR data in Fiacconi et al. (2017), we obtain a stable stellar as well as gaseous disk.

3.2. A Multi-component Primeval Disk Galaxy

Analyzing how and where star formation proceeds as the galaxy evolves led us to the conclusion that stars do not form only in a single plane or layer, but rather in multiple sub-units having various heights, radial extents, and relative orientations. To properly define a (thin) disk and other accompanying components, we applied the DBSCAN (Ester et al. 1996) clustering algorithm to our data set. The algorithm, which can be described as a special case of the friends-of-friends algorithm, as shown by Kwon et al. (2010), identifies the main disk body by using a density threshold to group particles (we choose a density threshold of roughly 1 $M_\odot$ pc^{-2} within 100 pc around each star), and then discards particles that are spatially separated from any of the identified groups. More specifically, a star particle belongs to a group if it encompasses 40 other stellar particles within a sphere of radius 100 pc. Particles that
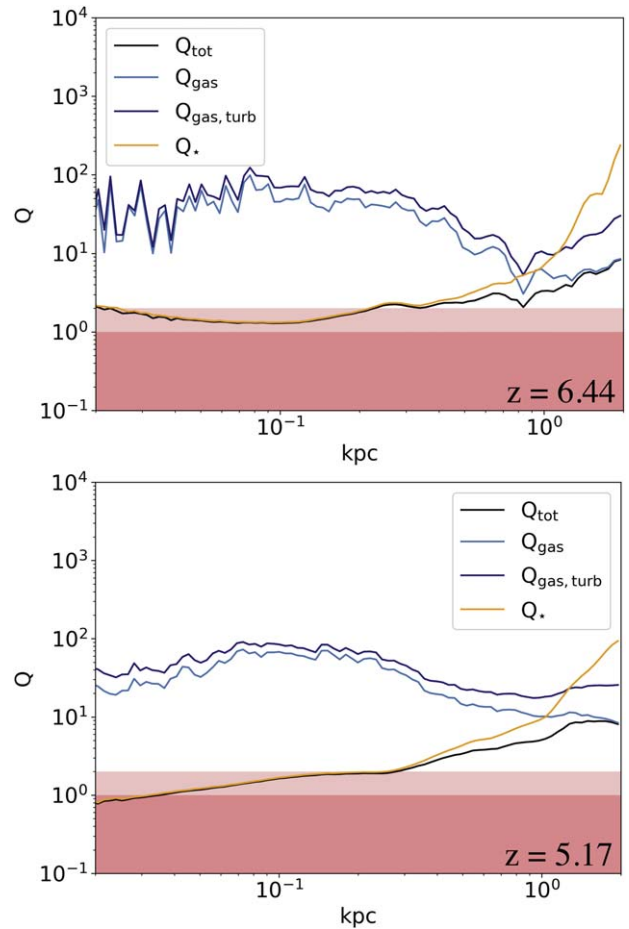
have fewer star particles than the nominal 40 within their own sphere, but are inside the sphere of another particle that satisfies the criterion, are also accounted for. In this way we identify sequences of mutually spatially connected particles, with a procedure conceptually similar to that of a gather/scatter kernel interpolation in SPH. Particles that do not define a group, or do not overlap with any group, are defined as isolated and discarded as background noise. We define the largest coherent group as the disk. The algorithm also finds other groups, not mutually connected with such largest group, which typically correspond to diffuse, three-dimensional features above and below the disk defined by the largest group. These are "bubbles" of extraplanar star formation (see this procedure in Figures 9, 10 and 11). Note that such bubbles are well resolved, encompassing up to about 4000 particles each. We remark that these pockets of extraplanar star formation would be barely resolved in conventional zoom-in simulations, which have a mass resolution more than one order of magnitude lower than that of GIGAERIS, and would then be discarded as background noise. We then proceed to quantify the structure of the disk of newborn stars discarding both the noise (individual particles) and the extraplanar bubbles, which will be studied in a future paper dedicated to diffuse baryonic components in the simulation.
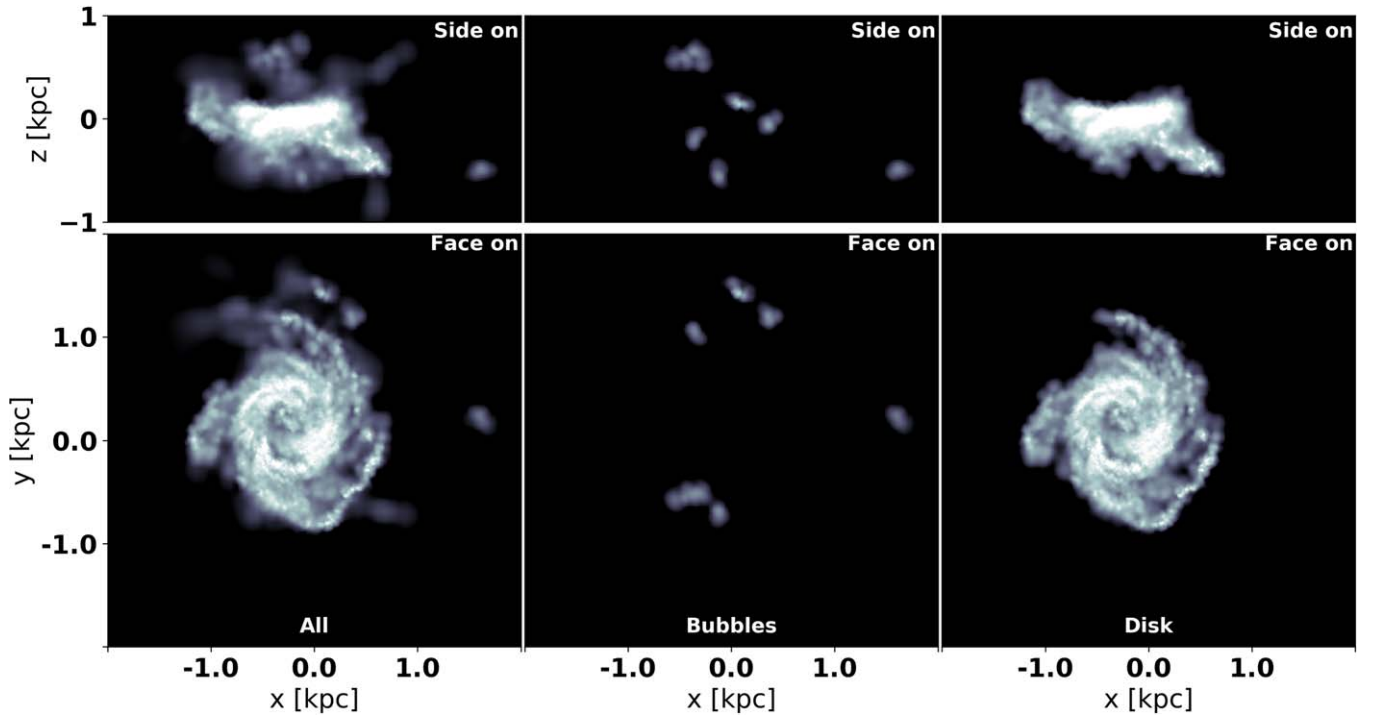
Figure 9. Stellar surface density "face on" (bottom panels) and "edge on" (top panels), with the total stellar angular momentum vector pointing along the z-axis, of the main GIGAERIS galaxy at $t = 0.48$ Gyr after the big bang ($z = 6.95$). The figure is divided in three vertical panels. From left to right: all newly born stars in that snapshot, only the stars born in individual groups ("bubbles"), and the disk stars.

In summary, we can outline the overall procedure to identify the newborn disk as follows.

1. Select a large box around the center of the galaxy [$-4\,\mathrm{kpc} < x < 4\,\mathrm{kpc}$, $-4\,\mathrm{kpc} < y < 4\,\mathrm{kpc}$, $-4\,\mathrm{kpc} < z < 4\,\mathrm{kpc}$].
2. Find the newborn stars within this region [$dt = 0.017$ Gyr].
3. Apply the DBSCAN algorithm to identify the main disk body as described above, discarding background noise and bubbles.
4. Recenter on the remaining disk stars and orient the disk such that the angular momentum vector is perpendicular to the xy-plane ("face on").

This procedure can be applied recurrently to analyze the distribution and kinematics of the stars identified in each snapshot. We determine the thickness via the vertical density profile at 80% of the enclosed mass estimated by

$$\rho(z) = C \operatorname{sech}^2\left(\frac{z - \mu}{z_\star}\right), \qquad (5)$$

with C being a normalization constant, μ the mean value of the vertical component of the disk, and $z_\star$ the disk thickness. Additionally, since we already know that the disk is not formed in a single disk-like layer but instead within a complex structure, we also performed a two-component sech^2 profile fit:

$$\rho(z) = C_1 \operatorname{sech}^2\left(\frac{z - \mu}{z_{\mathrm{thin}}}\right) + C_2 \operatorname{sech}^2\left(\frac{z - \mu}{z_{\mathrm{thick}}}\right), \qquad (6)$$

with C_1 and C_2 being normalization constants, μ again the mean z-value of the disk stars, and z_{thick} and z_{thin} the thick- and thin-disk scale heights, respectively. In Figure 12, we show the results of both fitting procedures. With this method, we are always able to find a thin-disk component independently from a single or double fit. The left-hand side clearly depicts that a single fit yields very good χ^2/ν values[7] (smaller than 3) and that all are below 300 pc. Therefore, we can conclude that a thin disk is always in existence, but can be hidden by ex situ formation or stellar accretion via consecutive galaxy mergers. We also want to mention that a two-component fit (Equation (6)) will likely lead to degenerate results, but since our results from both fits are consistent with each other and always display a thin disk, we do not further investigate this issue.

We then revisit the evolution of the kinematics of in situ stars by tracking them over time. Specifically, we identify ensembles of stars that are born at a given time in the disk, identified by DBSCAN, measure their $\langle v_\phi \rangle / \sigma_R$ at the initial time, and track these same stars until the end of the simulation. By repeating the procedure at each snapshot, we identify a set of coeval sub-components of the disk (coeval disks). The dynamics of the stars in these sub-disks can be perturbed by satellites or internal instabilities such as bars, but there is no contribution of ex situ stars by construction, given the way we identify the coeval sub-disks. Therefore, in Figure 13, we show the time evolution of $\langle v_\phi \rangle / \sigma_R$ for multiple co-evolving disks identified with DBSCAN. In contrast to Figure 6, we can see that once an individual sub-disk is formed it remains a kinematically cold structure, hence it is not heated or destroyed by any of the aforementioned mechanisms. In contrast, quite surprisingly the ratio $\langle v_\phi \rangle / \sigma_R$ increases with time in all cases. Moreover, the $\langle v_\phi \rangle / \sigma_R$ of the newly born stars (Figure 13) is always higher than the $\langle v_\phi \rangle / \sigma_R$ of the global galactic disk (Figure 6), which includes the contributions from all the coeval disks. The increase is largest

_____

[7] The χ^2 errors have been estimated by assuming a Poisson sampling noise.
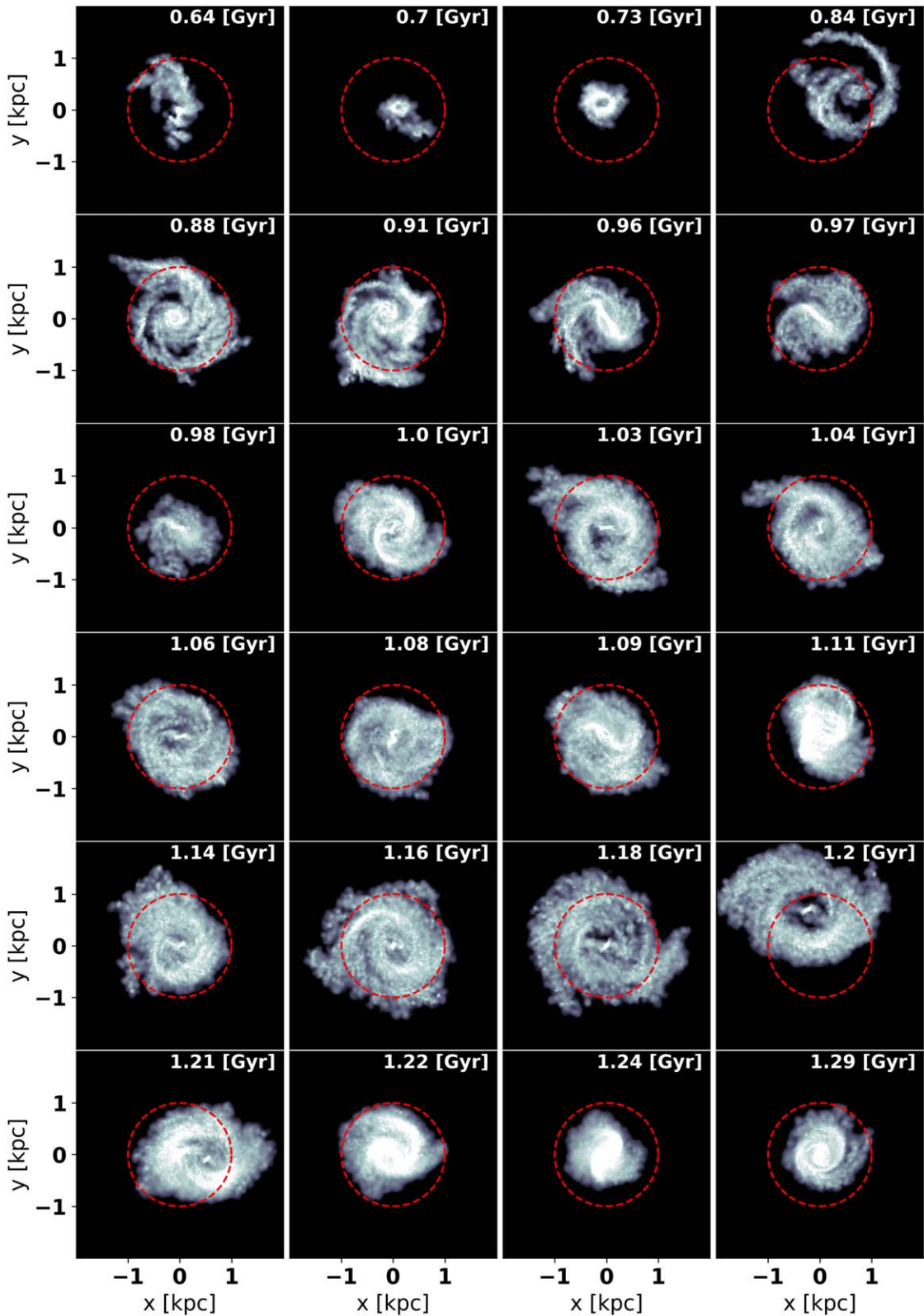
Figure 10. Surface density of the newly born stars (face on) of the main GIGAERIS galaxy as a time sequence. To make the evolution of the disk clearly visible, we added a red circle with a radius $r = 1$ kpc.

at the latest times. This suggests that what we are witnessing is indeed higher angular momentum disk components building up with time, a well established fact in cold DM (CDM) cosmogonies (e.g., Sokołowska et al. 2017), but also that, as such new higher angular momentum components

assemble, the stars belonging to previous coeval disks are not heated up significantly; rather, they increase their rotation speed as more mass is added in the disk itself, because kinetic energy has to increase if the system has to remain in equilibrium.
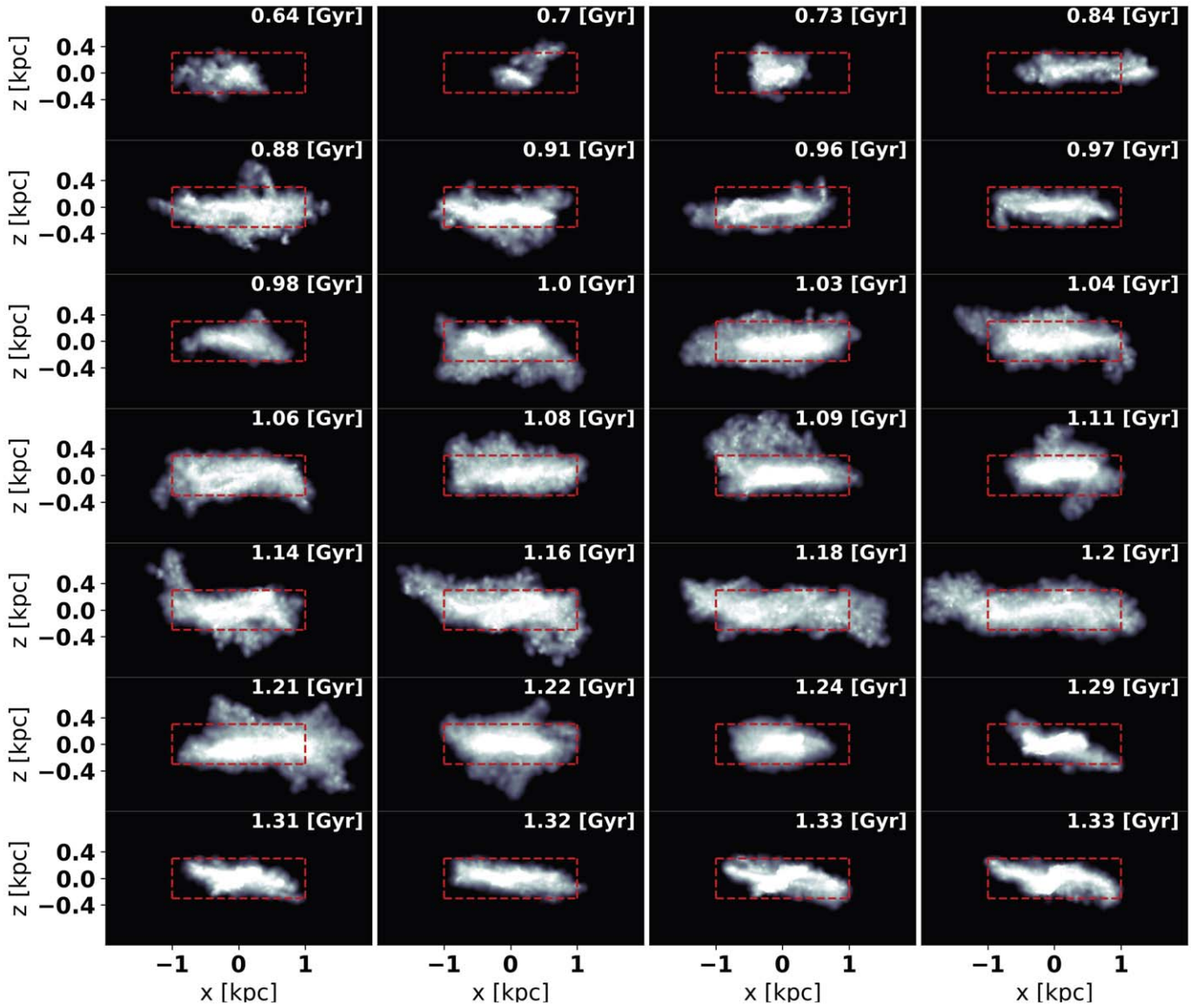
Figure 11. Surface density of the newly born stars (edge on) of the main GIGAERIS galaxy as a time sequence. The thin disk appears to exist in every snapshot, although we can observe a slight warp in some cases. The red box indicates a height of 600 pc and a width of 2 kpc.

Overall the picture that emerges is that the decrease of $\langle v_\phi \rangle / \sigma_R$ shown in Figure 6 is almost entirely due to an increasing contribution of higher-velocity dispersion stars added by accretion events, i.e., from ex situ stars, rather than being due to heating of the pre-existing in situ component. This essentially agrees with the notion, so far established at low redshift only, that disk heating is actually a rather mild dynamical driver of disk evolution, contrary to claims in early studies of galaxy–satellite interactions (Kazantzidis et al. 2009; Grand et al. 2016). The fact that, in Figure 13, the overall disk has a milder increase of $\langle v_\phi \rangle / \sigma_R$ reflects the fact that the angular momenta of the sub-disks are not aligned, so that, when they are superimposed, the net angular momentum around the mean rotation axis can only be smaller than that of the individual components (note that also for the global disk we are only considering in situ stars).

4. Discussion

In this work, we have shown that stars are assembled in a flattened disk component already at very high redshift, as early as $z \sim 8$, in a progenitor of a present-day Milky Way-sized galaxy halo. A thin disk is present until the end of the simulation, at $z \sim 4.4$, and results from subsequent episodes of star formation from newly accreted cold gas.

The implication is that, unless dynamical heating, internal or external, heats up considerably the entire early thin disk over the following several gigayears, a remnant old thin-disk component, with age > 10 Gyr, should be present in present-day massive spirals. Indeed this is in good agreement with new observations from the Gaia DR2 release, in which roughly 20%–30% of the oldest stars of the Milky Way, with a $[\mathrm{Fe/H}] \leqslant -2.5$ and thus born only 2–4 Gyr after the big bang (see El-Badry et al. 2018), are arranged in a thin rotating disk
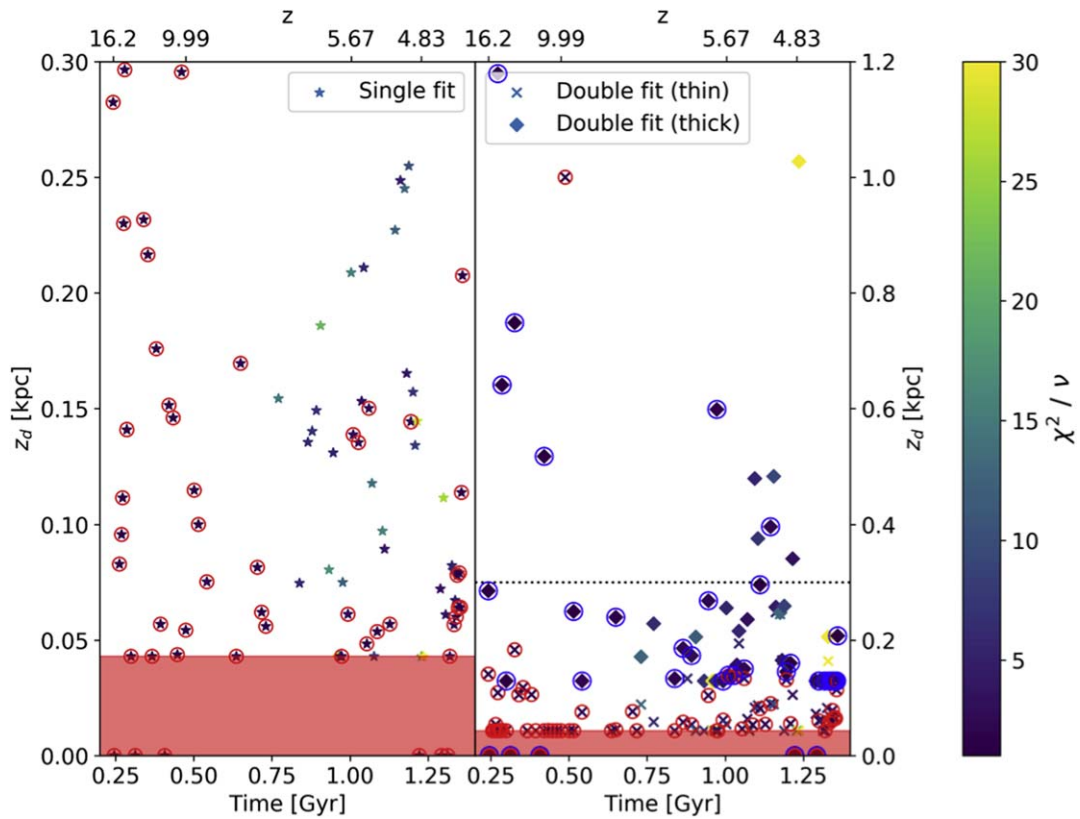
Figure 12. Characterization of disk thickness for newborn disk stars in various snapshots as a function of time. The left-hand panel shows the results of the single-profile fitting procedure to infer the height z_d using 80% of the enclosed mass. The right-hand panel depicts the outcome of the double-profile fitting procedure to infer the scale height z_d (crosses and rhombuses for the thin and thick component, respectively), again at 80% of the enclosed disk mass. The encircled values have a reduced χ^2 value between 1 and 3. The red shaded area indicates the softening length of the simulation and the black, horizontal dotted line on the right-hand side shows the maximum range of the left-hand plot.

(Sestito et al. 2020). The comparison with the present-day thick disk of the Milky Way is instead not possible, as both internal dynamical processes and accretion will occur from $z \sim 4$ to $z = 0$, which we cannot capture due to the limited evolutionary timescales probed by GIGAERIS. Therefore, it cannot be excluded that at least part of the primeval thin disk will contribute to the thick disk at a later time, or that it might evolve into a pseudobulge via disk instabilities (Guedes et al. 2013), which would match its compact radial size scale.

We also find that only a fraction of the stars that are present at redshift $z = 4.44$ are actually born in situ, the vast majority of them being born outside of the final stellar disk. We speculate that the primeval thin disk has been missed in former studies due to the latter fact combined with limited mass and spatial resolution. We argue that the GIGAERIS simulation portrays evidence that the formation mechanism of high-redshift disks is fundamentally analogous to that of low-redshift disks. With enough resolution to resolve the flow in the circumgalactic and interstellar medium down to scales of a few parsecs, radiative cooling does produce thin rotationally supported layers, out of which stars form, already at very high redshift, and naturally build up a stellar component in a relatively thin disk. A major difference with low redshift is that, due to the much smaller halo scale size, which reflects the nature of hierarchical structure formation in CDM, the angular momentum of accreting baryonic matter is lower at high redshift, resulting in an initially smaller disk aspect ratio. Yet the stellar kinematics that result are already typical of a thin disk, rather than of a thick disk or spheroid. Another difference relative to

low-redshift disks is that, owing to shorter infall times, filamentary accretion more frequently assembles sub-components of the disk whose planes have mutual inclinations. However, as shown by our DBSCAN analysis, these different coeval disks all have cold kinematics and, at least in the object under study, globally the kinematics is still that of a rotationally supported disk, albeit with somewhat hotter kinematics than some of the individual sub-components.

Since only a small fraction of the final stellar disk (at redshift $z = 4.44$) is made up of in situ stars, we further theorize that the bulk of the thick disk is created either due to constant accretion and (minor) merger events as described in Minchev et al. (2015) or due to internal heating mechanisms as described by Park et al. (2021). Nonetheless, the build-up and origin of the thick stellar disk will be the subject of future work.

Another zoom-in simulation with comparable mass and force resolution, and similar sub-grid physics, PONOS-HR, which follows the formation of a nearly one-order-of-magnitude more massive system, revealed a thicker disk, with a hotter interstellar medium, driven by powerful supernovae explosions. At a comparable redshift, $z \sim 6.5$, GIGAERIS has indeed a lower Toomre Q parameter, even when accounting for gas turbulence (Figure 8), relative to PONOS-HR (see Figure 9 in Fiacconi et al. 2017), and its stellar surface density profile is also significantly steeper in the inner kiloparsec region, whereas PONOS-HR exhibited an almost perfectly single exponential profile throughout (see Figure 7). Note also that the stellar mass is a factor of two larger in GIGAERIS at this time, despite the fact that the halo has a virial mass a factor of
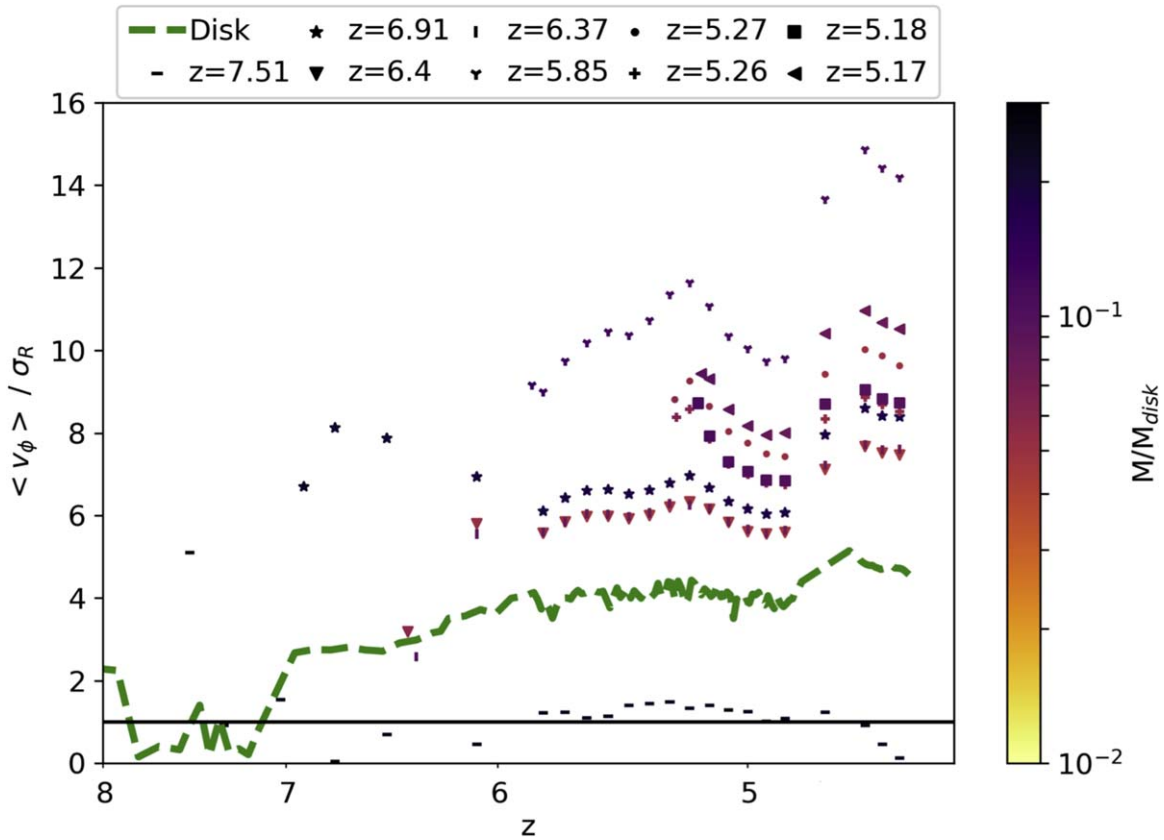
Figure 13. Kinematical evolution of coeval stellar disk sub-components identified by the DBSCAN algorithm. For any component, labeled by a birth time in the figure, the same stars are followed until the final redshift, hence they are coeval. We show their $\langle v_\phi \rangle / \sigma_R$ values as a function of time. The stars are tracked throughout the simulation and the associated disk is always realigned such that the angular momentum vector points toward the z-direction. The scatter-points are color-coded by the ratio of the cohorts mass to the total disk mass at the corresponding time step. It is obvious that the $\langle v_\phi \rangle / \sigma_R$ does not decrease as in Figure 6, but rather increases. With this method, we are not biased by ex situ formation and galaxy mergers and therefore obtain a larger $\langle v_\phi \rangle / \sigma_R$ value. The green line depicts the value for the total galactic disk and it can be seen that this value is always significantly lower than that of the individual coevolving disks. We also obtain high (and stable) values of $\langle v_\phi \rangle / \sigma_R$ as early as at redshift $z = 7$.

two lower compared to PONOS-HR. Overall the stellar disk in GIGAERIS is thus both more massive and more centrally concentrated. This suggests, thus, significant variation in galactic structure in galaxies that, at high redshift, have a rather similar stellar mass. Such diversity is likely due to different halo assembly history and cosmic web environment generating a different gas infall/accretion flow. Overall, it would seem that in PONOS-HR feedback has been more effective at suppressing the accumulation of baryons in the central region of the halo, thus maintaining a lower ratio of the stellar-to-halo mass. Nevertheless, even in PONOS-HR a disk component is clearly dominant, albeit more turbulent and kinematically hotter than in GIGAERIS. Whether these differences in the early disk assembly are typical between systems that are progenitors of massive spirals as opposed to massive isolated early-type galaxies cannot be assessed until a similarly detailed structural study will be possible in a larger sample of simulations. Another important aspect that will have to be investigated to understand the origin of these differences is the role of the warm/hot corona surrounding the early disk. This is born out of both shocks in the accretion flow and feedback. Sokołowska et al. (2018) have shown that stronger feedback leads to a faster build-up of the corona, which then partially suppresses cold flows earlier, thus limiting the growth of the baryonic disk. Major galaxy mergers have also been shown to enhance the effect of feedback, implying that the merging

history of the galaxy plays a role (Sokołowska et al. 2018). Future analysis will assess if feedback, perhaps due to the different merging history, has a stronger impact in PONOS-HR than in GIGAERIS, as suggested by the larger fraction of warm/hot gas ($T > 5 \times 10^4$ K) in the disk of the former. Notably, PONOS-HR undergoes more and more recent major mergers ($q > 0.25$), indeed as many as three after $z = 15$ as opposed to only one in the case of GIGAERIS, and the last one is also more recent, near $z = 7$ as opposed to $z = 13$ in GIGAERIS.

We also mention that we cannot present any statistics on how often such a disk forms in a typical galaxy due to our small sample size. Given the resolution and particle numbers in this study it is not feasible to re-simulate this galaxy nor to focus on another galaxy within the simulated box. For larger statistics, we refer the reader to the study done by Park et al. (2021).

Finally, we also explored the detectability of such a high-redshift disk with the recently launched James Webb Space Telescope (JWST). In Figure 14, we show the surface density maps in ideal NIRCam-sw resolution (see Table 1) as well as the star formation surface density (see first and second columns). We can apply the relation between the star formation rate and the luminosity in the UV band given by (see Kennicutt 1998)

$$\mathrm{SFR}\left[\frac{M_\odot}{\mathrm{yr}}\right] = 1.4 \times 10^{-28} L_{\mathrm{UV}}\left[\frac{\mathrm{erg}}{\mathrm{sHz}}\right]. \tag{7}$$
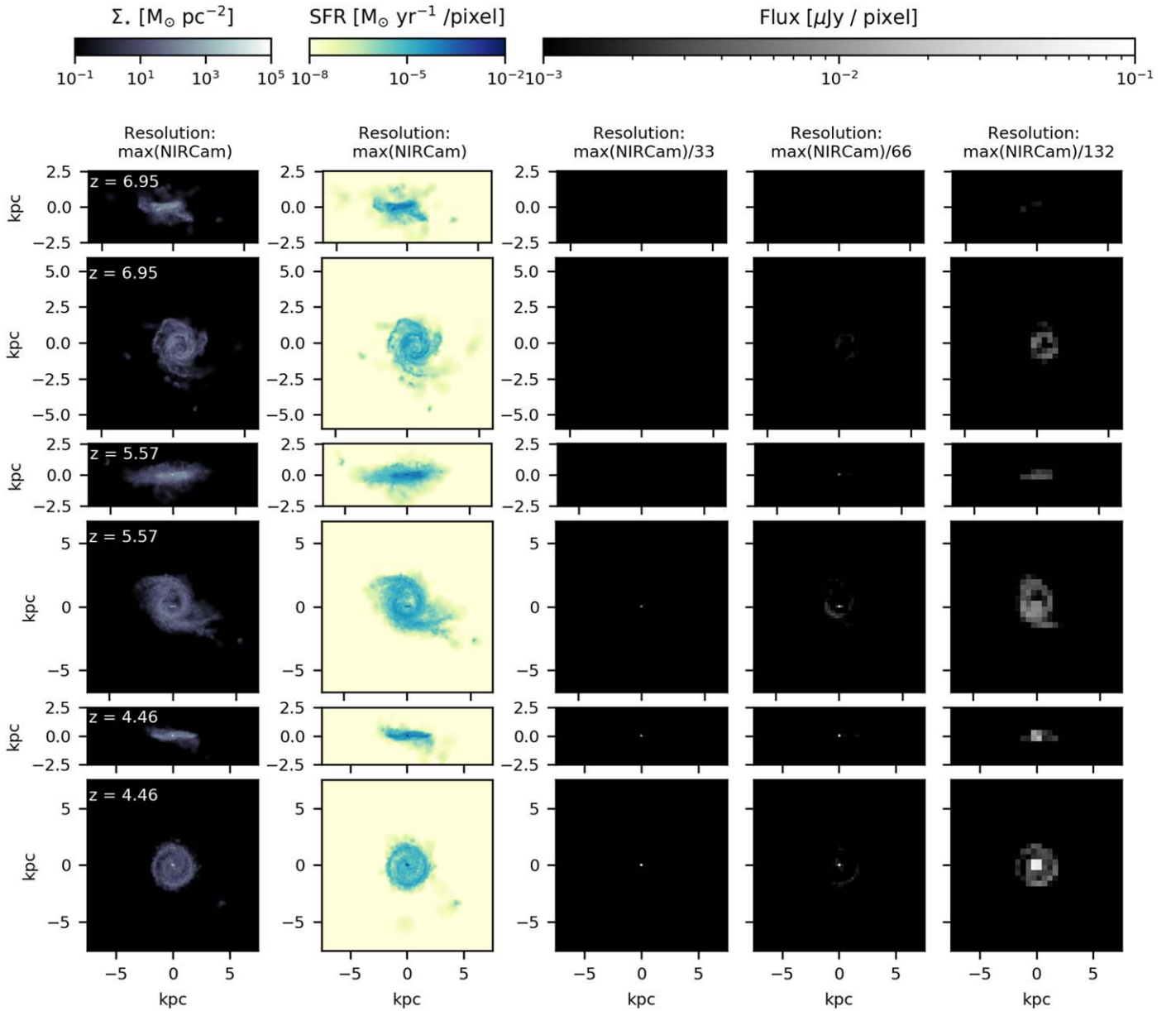
Figure 14. Mock observations with the NIRCam camera of the James Webb Space Telescope (JWST) at short-wavelength imaging. On the left-hand side we show the theoretical surface density of the galaxy at three different redshifts, $z = 6.95$, 5.57, and 4.46 (from top to bottom), with a spatial resolution comparable to the NIRCam resolution. The second column shows the star formation rate per resolution element ("pixel"). Afterwards, we transform the star formation rate to μJy using the relations given by Kennicutt (1998) and combine as many pixels as necessary to obtain a reasonable flux (see the last three columns). In our example, we used an exposure time of 7 cycles (roughly 3 h 49 min) and a signal-to-noise ratio of roughly 5 at 10^{-2} μJy. We can see that all disks, which are depicting newborn stars, can be reasonably resolved at all redshifts. Therefore, the JWST will be an ideal instrument to find high-redshift disk galaxies.

Afterwards, we transformed $L_{\rm UV}$ to Jy and calculated the flux in μJy:

$$\text{flux}[\,\mu\text{Jy}] = (1 + z)\frac{L_{\rm UV}}{4\pi D_L^2} \cdot 10^6, \qquad (8)$$

with $D_{\rm L}$ being the luminosity distance in megaparsecs. Furthermore, with the help of the online Exposure Time Calculator for the JWST,[8] we calculated that, with the NIRCam-sw camera and an exposure time of roughly 3 h 49 min, we can obtain a signal-to-noise ratio of 5 for a flux of 10^{-2} μJy. The last three panels of Figure 14 show the results of

summing up 33, 66, and 132 neighboring pixels in the NIRCam-sw camera in order to obtain the necessary flux. As can be seen, the disk would be detectable, in some cases also edge-on, not only toward the end of the simulation, at $z \sim 4.4$, but also at much higher redshift, $z \sim 7$. This opens the exciting prospect of directly testing the results of our numerical simulation. Since we have modeled a galaxy that is a typical star-forming galaxy at the relevant redshift, a non-detection of a clear disk component may be in favor of an irregular or distorted galactic structure. This could point to some issue in the sub-grid physics models, as the balance between radiative cooling and feedback is crucial to determine whether a dominant kinematically cold disk component forms or not (e.g., Sokołowska et al. 2017).

---

[8] https://jwst.etc.stsci.edu/

Table 1
Four Cameras of the James Webb Space Telescope (Miri, NIRCam-lw, NIRCam-sw, and NIRISS) and Their Wavelength Bands, Square area, Resolution Per Pixel, and Geometry

Name	Wavelength (μm)	Area (arcmin^2)	Resolution ($''$/pix)	Geometry ($'' \times ''$)
MIRI	5.6–26.5	3.1	0.11	74×113
NIRCam:				
lw	2.4–5.0	9.7	0.063	264×264
sw	0.6–2.3	9.7	0.031	264×264
NIRISS	0.8–5.0	4.84	0.065	133×133

5. Summary and Conclusion

The main results of our high-resolution cosmological zoom-in simulation of a Milky Way-sized galaxy halo can be summarized as follows.

1. In our simulated galaxy a thin disk is always present since the earliest assembly stage. Such disk is kinematically cold, namely the rotation clearly dominates over the stellar velocity dispersion, as in present-day disks of spiral galaxies.

2. The heating of in situ stars by internal dynamical instabilities and external perturbations is negligible. Rather, sub-disks formed at different epochs remain kinematically cold, or even exhibit an increase of the $\langle v_\phi \rangle / \sigma_R$ ratio. The overall decrease of $\langle v_\phi \rangle / \sigma_R$ observed as time progresses is thus resulting primarily from the contribution of ex situ stars.

3. The disk develops a multi-component structure already early on, as the stellar distribution thickens gradually primarily due to external perturbations or direct stellar accretion from infalling satellites. Ex situ stars incorporated by accretion provide the main contribution to the vertically extended component of the disk, which is consistent with them being kinematically hotter.

4. There is no "upside-down" disk formation, rather a continuous "inside-out" growth of a thin-disk component. A stellar disk formed "upside-down" if the early progenitor of the disk formed hot. This happens because the star-forming gas can have a high velocity dispersion and still be Toomre unstable at high redshift, due to the high gas mass fraction. Indeed, while a thin disk with vertical extent below 0.5 kpc is present since $z > 8$, the disk aspect ratio is larger than in a present-day disk of a spiral galaxy as its initial radial extent is very compact (about a kiloparsec) due to the lack of high angular momentum material at high redshift. We propose that this disk can be the seed of today's thin and old Milky Way's stellar disk.

5. With the advent of the JWST, as we showed in Figure 14, we will be able to observe and characterize high-redshift galaxies that are formed by assembling a sequence of thin, kinematically cold stellar disks, and hence test our predictions and potentially set new constraints on the physics of galaxy formation at the earliest epochs.

The scenario of disk formation that emerges for the early assembly phase of a massive spiral as that modeled here seems at odds with the widely adopted "upside-down" disk formation model (e.g., Bird et al. 2013, 2021), in which disks are born thick and the thin disk builds up later from kinematically colder, higher angular momentum gas accreting at lower redshift. However, close inspection of the evolution of thickness in the ERISLE run reported in Bird et al. (2013) shows that, in the inner disk at $R < 1$ kpc, the stars older than 10 Gyr are characterized by a scale height lower than 500 pc, while the inner disk becomes thicker with time. Since it is this inner disk less than 2 kpc in size that is in place at the redshifts considered in this paper, our results are after all not in conflict. However, due to the lack of resolution, both spatial and mass, neither Bird et al. (2013) nor other works studied the inner disk, hence their conclusions on "upside-down" formation are driven by the later formation phase of the galaxy. Instead, here we clearly showed that, once numerical resolution is up to the challenge, a thin disk is seen to form even at $z \sim 7$–8, essentially as soon as the galactic disk begins to assemble. This of course has important implications for upcoming observations of the stellar component of high-redshift galaxies by the JWST and other instruments.

One may wonder which component of the present-day Milky Way, or of spiral galaxies in general, corresponds to the primeval thin disk identified here. We argue that the primeval thin disk in our simulation provides a natural explanation for the oldest thin-disk component revealed by the Gaia DR2 release, but it is also possible that part of the primeval inner disk would evolve into a disky pseudobulge (see also Guedes et al. 2013), which is a ubiquitous component in the central regions of massive late-type galaxies (nearly all of those in the Local Volume have such a component; see Kormendy & Ho 2013). Previous work had already found that pseudobulges could form at $z > 3$ in disk galaxies, but had attributed that mostly to the evolution of an early bar (Guedes et al. 2013). In contrast, we believe that at least a fraction of the pseudobulge stars can originate in situ from pre-existing stars that formed in the primeval compact, kinematically cold disk configuration. The presence of an old pseudobulge component in local late-type spiral galaxies is fairly well established observationally (Kormendy & Bender 2019). The latter pseudobulges, though, are often vertically extended configurations, so-called peanut-like bulges, which are consistent with bar-like components dynamically heated by a buckling instability (Debattista et al. 2006). Whether dynamical heating occurred at low redshift for the inner disk stars in our simulation cannot be probed in GIGAERIS. It is possible that present-day pseudobulges may hide a kinematically colder component with age >10 Gyr. This could be tested with much more accurate measurements of stellar kinematics in the heart of the Milky Way and other local spirals, which will be soon available with the LSST/Vera Rubin Observatory.

The data that support the findings of this study are available upon reasonable request from the authors.

ORCID iDs

Tomas Tamfal ● https://orcid.org/0000-0003-1773-9349
Lucio Mayer ● https://orcid.org/0000-0002-7078-2074
Thomas R. Quinn ● https://orcid.org/0000-0001-5510-2803
Arif Babul ● https://orcid.org/0000-0003-1746-9529
Piero Madau ● https://orcid.org/0000-0002-6336-3293
Pedro R. Capelo ● https://orcid.org/0000-0002-1786-963X
Sijing Shen ● https://orcid.org/0000-0001-8523-1171

References

Abadi, M. G., Navarro, J. F., Steinmetz, M., & Eke, V. R. 2003, ApJ, 591, 499
Ardila, F., Huang, S., Leauthaud, A., et al. 2021, MNRAS, 500, 432
Barnes, J., & Hut, P. 1986, Natur, 324, 446
Bird, J. C., Kazantzidis, S., Weinberg, D. H., et al. 2013, ApJ, 773, 43
Bird, J. C., Loebman, S. R., Weinberg, D. H., et al. 2021, MNRAS, 503, 1815
Bortolas, E., Capelo, P. R., Zana, T., et al. 2020, MNRAS, 498, 3601
Debattista, V. P., Mayer, L., Carollo, C. M., et al. 2006, ApJ, 645, 209
Dehnen, W., & Aly, H. 2012, MNRAS, 425, 1068
Di Matteo, P., Lehnert, M. D., Qu, Y., & van Driel, W. 2011, A&A, 525, L3
Efstathiou, G., & Jones, B. J. T. 1980, ComAp, 8, 169
El-Badry, K., Quataert, E., Wetzel, A., et al. 2018, MNRAS, 473, 1930
Ester, M., Kriegel, H.-P., Sander, J., & Xu, X. 1996, in Proc. of the Second Int. Conf. on Knowledge Discovery and Data Mining, KDD'96 (Palo Alto, CA: AAAI Press), 226
Ewald, P. P. 1921, AnP, 369, 253
Ferland, G. J., Fabian, A. C., & Johnstone, R. M. 1998, AAS Meeting Abstracts, 193, 38.13
Ferland, G. J., Porter, R. L., van Hoof, P. A. M., et al. 2013, RMxAA, 49, 137
Fiacconi, D., Mayer, L., Madau, P., et al. 2017, MNRAS, 467, 4080
Garrison-Kimmel, S., Boylan-Kolchin, M., Bullock, J. S., & Lee, K. 2014, MNRAS, 438, 2578
Garrison-Kimmel, S., Wetzel, A., Hopkins, P. F., et al. 2019, MNRAS, 489, 4574
Gill, S. P. D., Knebe, A., & Gibson, B. K. 2004, MNRAS, 351, 399
Gilmore, G., Wyse, R. F. G., & Kuijken, K. 1989, ARA&A, 27, 555
Governato, F., Brook, C., Mayer, L., et al. 2010, Natur, 463, 203
Grand, R. J. J., Springel, V., Kawata, D., et al. 2016, MNRAS, 460, L94
Guedes, J., Callegari, S., Madau, P., & Mayer, L. 2011, ApJ, 742, 76
Guedes, J., Mayer, L., Carollo, M., & Madau, P. 2013, ApJ, 772, 36
Haardt, F., & Madau, P. 2012, ApJ, 746, 125
Hafen, Z., Faucher-Giguère, C.-A., Anglés-Alcázar, D., et al. 2019, MNRAS, 488, 1248
Hahn, O., & Abel, T. 2011, MNRAS, 415, 2101
Hodge, J. A., Smail, I., Walter, F., et al. 2019, ApJ, 876, 130
Hopkins, P. F., Wetzel, A., Kereš, D., et al. 2018, MNRAS, 480, 800
Inoue, S., Dekel, A., Mandelker, N., et al. 2016, MNRAS, 456, 2052
Jetley, P., Gioachin, F., Mendes, C., Kale, L. V., & Quinn, T. 2008, in IEEE Int. Symp. on Parallel and Distributed Processing (Piscataway, NJ: IEEE), 1
Jetley, P., Wesolowski, L., Gioachin, F., Kalé, L. V., & Quinn, T. R. 2010, Proceedings of the 2010 ACM/IEEE International Conference for High Performance Computing, Networking, Storage and Analysis, SC '10 (USA: IEEE Computer Society), 1
Jurić, M., Ivezić, Ž., Brooks, A., et al. 2008, ApJ, 673, 864
Kaufmann, T., Mayer, L., Wadsley, J., Stadel, J., & Moore, B. 2007, MNRAS, 375, 53
Kazantzidis, S., Zentner, A. R., Kravtsov, A. V., Bullock, J. S., & Debattista, V. P. 2009, ApJ, 700, 1896
Keller, B. W., Wadsley, J., Benincasa, S. M., & Couchman, H. M. P. 2014, MNRAS, 442, 3013
Kennicutt, R. C. J. 1998, ARA&A, 36, 189
Knollmann, S. R., & Knebe, A. 2009, ApJS, 182, 608
Kormendy, J., & Bender, R. 2019, ApJ, 872, 106
Kormendy, J., & Ho, L. C. 2013, ARA&A, 51, 511
Kretschmer, M., Dekel, A., & Teyssier, R. 2022, MNRAS, 510, 3266
Kroupa, P. 2001, MNRAS, 322, 231
Kwon, Y., Nunley, D., Gardner, J., et al. 2010, in Scientific and Statistical Database Management, 22nd International Conference, SSDBM 2010, Vol. 6187, ed. M. Gertz & B. Ludäscher (Berlin: Springer), 132
Le Fèvre, O., Béthermin, M., Faisst, A., et al. 2020, A&A, 643, A1
Mayer, L., Governato, F., & Kaufmann, T. 2008, ASL, 1, 7
Meng, X., & Gnedin, O. Y. 2021, MNRAS, 502, 1433
Meng, X., Gnedin, O. Y., & Li, H. 2019, MNRAS, 486, 1574
Menon, H., Wesolowski, L., Zheng, G., et al. 2015, ComAC, 2, 1
Meza, A., Navarro, J. F., Abadi, M. G., & Steinmetz, M. 2005, MNRAS, 359, 93
Minchev, I., Martig, M., Streich, D., et al. 2015, ApJL, 804, L9
Neeleman, M., Prochaska, J. X., Kanekar, N., & Rafelski, M. 2020, Natur, 581, 269
Park, M. J., Yi, S. K., Peirani, S., et al. 2021, ApJS, 254, 2
Planck Collaboration, Ade, P. A. R., Aghanim, N., et al. 2016, A&A, 594, A13
Pontzen, A., Governato, F., Pettini, M., et al. 2008, MNRAS, 390, 1349
Purcell, C. W., Kazantzidis, S., & Bullock, J. S. 2009, ApJL, 694, L98
Quinn, P. J., Hernquist, L., & Fullagar, D. P. 1993, ApJ, 403, 74
Rizzo, F., Vegetti, S., Powell, D., et al. 2020, Natur, 584, 201
Romeo, A. B. 1994, A&A, 286, 799
Romeo, A. B., & Falstad, N. 2013, MNRAS, 433, 1389
Romeo, A. B., & Wiegert, J. 2011, MNRAS, 416, 1191
Santistevan, I. B., Wetzel, A., Sanderson, R. E., et al. 2021, MNRAS, 505, 921
Sestito, F., Martin, N. F., Starkenburg, E., et al. 2020, MNRAS, 497, L7
Shen, S., Madau, P., Guedes, J., et al. 2013, ApJ, 765, 89
Shen, S., Wadsley, J., & Stinson, G. 2010, MNRAS, 407, 1581
Sokołowska, A., Babul, A., Mayer, L., Shen, S., & Madau, P. 2018, ApJ, 867, 73
Sokołowska, A., Capelo, P. R., Fall, S. M., et al. 2017, ApJ, 835, 289
Stinson, G., Seth, A., Katz, N., et al. 2006, MNRAS, 373, 1074
Tasca, L. A. M., Le Fèvre, O., Hathi, N. P., et al. 2015, A&A, 581, A54
Toomre, A. 1964, ApJ, 139, 1217
Villalobos, Á., & Helmi, A. 2008, MNRAS, 391, 1806
Wadsley, J. W., Keller, B. W., & Quinn, T. R. 2017, MNRAS, 471, 2357
Wendland, H. 1995, Adv. in Comput. Math, 4, 389
Wetzel, A. R., Hopkins, P. F., Kim, J.-H., et al. 2016, ApJL, 827, L23
White, S. D. M., & Rees, M. J. 1978, MNRAS, 183, 341
Wyse, R. F. G. 2001, in ASP Conf. Ser. 230, Galaxy Disks and Disk Galaxies, ed. J. G. Funes & E. M. Corsini (San Francisco, CA: ASP), 71
Wyse, R. F. G., Gilmore, G., Norris, J. E., et al. 2006, ApJL, 639, L13